RESEARCH ARTICLE

Energy & Environmental Materials WILEY

Proton Exchange Membrane Water Electrolyzer

Comprehensive Analysis of the Degradation Phenomena of Proton Exchange Membrane Water Electrolyzers with Iridium on Antimony Tin Oxide Anodes

Sambal Shashank Ambu, Nikolai Utsch, Tobias Morawietz, Maria Retuerto, Sergio Rojas, Oleg Usoltsev, Miriam Goll, Daniel García Sanchez, Andreas Glüsen, Aldo Saul Gago, Seyed Schwan Hosseiny, and Kaspar Andreas Friedrich*

Proton exchange membrane water electrolysis (PEMWE) has emerged as one of the most promising technologies for large hydrogen (H_2) production from renewable electricity. However, using iridium (Ir) in large quantities is a roadblock in the widespread expansion of this technology. One strategy to reduce Ir loading in the anode is the use of an electroceramic support material. This study examines the structural and electrochemical evolution of Ir on antimony tin oxide (Ir/ATO) anodes under extended operation. Initial electrochemical performance demonstrates that low-loaded Ir/ATO (0.2 mg_{Ir} cm^{-2}) can achieve a competitive current density of 2.82 A cm^{-2} at 2 V, comparable to state-of-the-art PEMWE catalysts. However, extended operation leads to a minimal but gradual decline in catalytic activity. Postmortem analysis reveals changes in porosity and pore distribution, while atomic force microscopy (AFM) studies indicate ionomer degradation in the anode catalyst layer (ACL). Transmission electron microscopy (TEM) reveals the dissolution of oxides of Sb and Sn from the support material. Furthermore, X-ray photoelectron spectroscopy (XPS) and X-ray absorption spectroscopy (XAS) confirmed the oxidation of metallic Ir (Ir^0) to $IrOx_x{\cdot}OH_y$ species before and after operation. Understanding degradation in low-Ir PEMWEs is key to improving long-term stability. These results highlight the need for support stabilization and catalyst structuring to ensure durable performance.

1. Introduction

The move toward a future low-carbon energy landscape can be realized with the integration of hydrogen in the energy mix.[1] In past years, there has been a heightened focus on water electrolysis coupled with renewable electricity as a critical technology for green hydrogen production.[2] Among the available technologies, proton exchange membrane water electrolysis (PEMWE) is highly suited for integration with variable renewable energy sources such as solar and wind.[3] PEMWE offers several advantages over traditional alkaline electrolysis, including system compactness, its capacity to operate at high current densities, a high dynamic range, high operational pressures, and high purity of gases, which make it increasingly favorable for large-scale hydrogen production.[4,5] Despite all these advantages, a major roadblock in scaling PEMWE technology lies in its dependence on noble metal catalysts. The acidic environment and operational demands of PEMWE necessitate the use of platinum (Pt) at the cathode and iridium (Ir) at the anode, which are used to facilitate the hydrogen evolution reaction and oxygen evolution

S. S. Ambu, Dr. M. Goll, Dr. S. S. Hosseiny
Cutting-Edge Nanomaterials UG (Haftungsbeschränkt), 49626, Berge, Germany
S. S. Ambu, Prof. K. A. Friedrich
Institute of Building Energetics, Thermal Engineering and Energy Storage (IGTE), University of Stuttgart, 70569, Stuttgart, Germany
S. S. Ambu, Dr. T. Morawietz, Dr. D. García Sanchez, Dr. A. S. Gago, Prof. K. A. Friedrich
Department of Electrochemical Energy Technology, Institute of Engineering Thermodynamics, German Aerospace Center (DLR), 70569, Stuttgart, Germany
E-mail: aldo.gago@dlr.de
Dr. N. Utsch, Dr. A. Glüsen
Forschungszentrum Juelich GmbH, Institute of Energy Technologies, IET-4, Electrochemical Process Engineering, 52425, Juelich, Germany
Dr. T. Morawietz
Faculty of Science, Energy and Building Services, Esslingen University of Applied Sciences, 73728, Esslingen am Neckar, Germany
Dr. M. Retuerto, Prof. S. Rojas
Grupo de Energía y Química Sostenibles, Instituto de Catálisis y Petroleoquímica (CSIC), C/Marie Curie 2, 28049, Madrid, Spain
Dr. O. Usoltsev
ALBA Synchrotron Light Source, Carrer de La Llum 2–26, 08290 Cerdanyola Del Vallès, Barcelona, Spain
Dr. M. Goll
Cellcentric GmbH & Co. KG, Neue Str. 95, 73230, Kirchheim unter Teck, Germany
The ORCID identification number(s) for the author(s) of this article can be found under https://doi.org/10.1002/eem2.70242.

DOI: 10.1002/eem2.70242

reaction (OER), respectively. The scarcity and excessive cost of these metals, particularly Ir, present major challenges for scaling up PEMWE technology. The realistic availability of Ir for water electrolysis usage is ~1.5 metric tons (20% of the world's annual Ir production).[6] These challenges are further exacerbated by persistent supply chain bottlenecks. As a byproduct of Pt extraction, Ir is not mined independently but recovered during the refining of platinum group metals (PGMs), predominantly in a handful of mining operations located in South Africa and Russia.[7] This intrinsic dependency on Pt production tightly links Ir availability to fluctuations in Pt market dynamics and mining outputs, introducing an additional layer of supply risk and unpredictability. Furthermore, governance-related issues including weak regulatory oversight, lack of transparency in mining operations, socio-environmental concerns, and geopolitical instability in major producing countries compound these risks. These critical mineral governance challenges hinder the development of secure, diversified, and resilient supply chains. The result is increased market volatility and constrained access to Ir, a material essential for green hydrogen production and other emerging clean energy technologies.[4,8–10]

While efforts to reduce Pt loading have proven effective while maintaining performance and stability,[11] similar advancements for Ir remain elusive, highlighting a key hurdle in PEMWE catalyst design. Current industrial PEMWEs typically operate with Ir loadings ranging between 1.2 and 2.0 mg_{Ir} cm^{-2}[6,12] to overcome the inherently sluggish kinetics of OER; however, such a high Ir usage is neither sustainable nor economically feasible at scale. Attempts to decrease the Ir loading with benchmark catalyst (usually IrO_2) in PEMWEs lead to a thin anode catalyst layer (ACL).[11] The homogeneous thin catalyst layers are not only difficult to make but also lead to contact problems with the porous transport layer (PTL).[13,14] Moreover, such thin layers are susceptible to crack formation, leading to fragmentation, in-plane disconnection, and the creation of electrochemically inactive regions.[15]

One successful approach to reducing the Ir amount is to disperse the particles on a high surface area support.[16] This approach increases the surface area by reducing particle size, thereby enhancing the number of catalytically active sites. Traditional carbon supports are used to disperse the platinum, but cannot be used as support materials in the anode due to their corrosion in high anodic potential and oxidative environment of PEMWE.[17] As a result, alternative support materials with high stability under acidic and oxidative conditions, such as TiO_2,[18] Magneli phase,[19] SnO_2,[20] Sb-doped SnO_2,[21] and TiC[22] along with many other transition metal oxides,[23] carbides,[24,25] and oxynitrides.[26]

Among these, antimony tin oxide (ATO) is one of the most promising candidates due to its relatively high electrical conductivity[27] and its low price.[28] Various groups have studied ATO as support for Ir catalyst. Oh et al.[29] have observed metal–metal oxide support interaction (MMOSI) in the IrO_x/ATO catalyst support couple, which mitigates the rate and extent of Ir oxidation and Ir dissolution at anodic oxidation potentials. Similarly, Hartig-Weiss et al.[30] have synthesized Ir/ATO catalysts with maximum synergistic effect with exceptional OER activity. Saveleva et al.[31] have highlighted the ATO stabilizing effect, ascribed to oxygen spillover mechanisms that help in stabilizing Ir active sites. Conversely, some studies, such as those by Khan et al., have reported minimal evidence of metal-support interactions, indicating that further investigation is needed to clarify the conditions under which these effects are significant.[32] Similarly, Ir nano dendrites (Ir-ND), while intrinsically more active than Ir black catalyst due to their morphology, demonstrated an improved activity when deposited on ATO compared to Ir/C or Ir-ND supported on carbon.[33,34] Despite the relatively high conductivity of ATO, a loading of more than 40 wt.% of Ir was found to be necessary in Ir tin oxide alloys.[35] Puthiyapura et al.[21] have studied the influence of different loadings of Ir deposited on commercial ATO nanoparticles and observed better performance with Ir loading of at least 60 wt.%. However, Geiger et al.[36] have reported the stability limits of Sb_2O_5:SnO_2, where they found Sb_2O_5 and SnO_2 oxides are stable within $0.36\ V_{RHE} < E < 1.1\ V_{RHE}$ and $-0.29\ V_{RHE} < E < 1.45\ V_{RHE}$, respectively, in a scanning flow cell experiment.[36]

While many studies have concentrated on half-cell testing, comprehensive investigations of Ir/ATO anodes in complete PEMWE systems are limited, particularly at low-Ir loadings.[21,33,37] There is also a lack of in-depth analysis regarding the morphological, compositional, and chemical structure evolution of Ir/ATO post-operation in a PEMWE cell. In this work, we address these gaps by conducting a thorough investigation from Ir/ATO catalyst synthesis and low-loaded single-cell PEMWE testing to extensive post-operation characterization with the aim of elucidating the degradation mechanisms of the Ir/ATO anode layer and catalyst particles under realistic operating conditions and their implications on long-term durability.

2. Results and Discussion

2.1. Catalyst Powder Morphology and Structure

Figure 1a shows the distribution of the synthesized Ir/ATO catalyst studied by scanning electron microscopy (SEM) using backscattered electron mode for enhanced contrast between Ir and support. The image reveals that Ir nanoparticles (bright areas) are well-dispersed on the surface of the ATO (gray areas) in small clusters. The loading of Ir on ATO was determined by energy dispersive X-ray (EDX) analysis, and the loading of Ir on support was found to be 47.94 ± 3.05 wt.% (Table S1, Supporting Information). The X-ray powder diffraction (XRD) of the powder catalyst was performed (Figure 1b). The XRD reflections of Ir and ATO phases are different. Three broad peaks at $2\theta = 40.5°$, 46.5°, and 68.9° can be indexed to the (111), (200), and (220) Miller indices corresponding to interplanar distances of the metallic Ir in the face-centered cubic structure.[33] The very broad reflections indicate the small size of the X-ray crystalline domain of the Ir nanoparticles. Also, the presence of multiple broad reflections suggests the polycrystalline nature of Ir, consisting of numerous small, randomly oriented crystallites. This polycrystallinity is advantageous for catalytic applications, as it increases the density of grain boundaries, and these high-energy sites might act as active sites for reactions.[38] On the other hand, the ATO phase shows sharp reflections at $2\theta = 33.6°$, 37.7, 51.5°, etc., indicating a tetragonal (rutile-like) structure. The narrow reflections indicate large crystalline domains of ATO, especially in comparison to Ir. We determined the crystal structures of both phases using Rietveld refinement. ATO was refined in the tetragonal rutile $P4_2/mnm$ space group with cell parameters $a = b = 4.73093(9)$ Å, $c = 3.18277(7)$ Å, and $V = 71.236(2)$ Å^3, similar to the previously published ATO crystal structure.[39]

Metallic Ir was refined in the cubic Fm-3m space group with cell parameters $a = 3.835(1)$ Å and $V = 56.41(3)$ Å^3, also similar to the previously published Ir structure.[40]

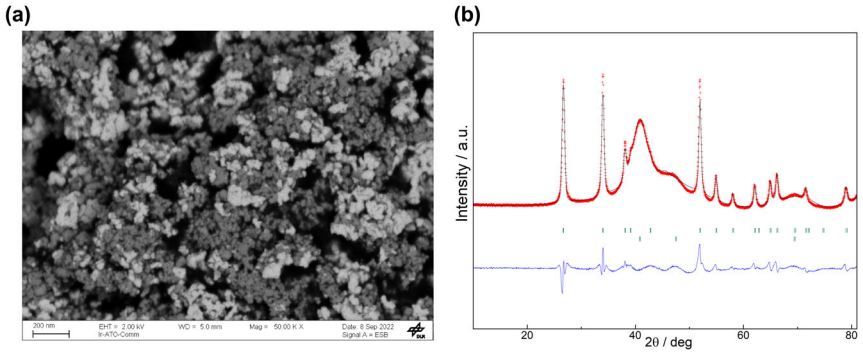

Figure 1. a) Scanning electron microscopy (SEM) images of the Ir/ATO at 50 000× with scale representing 200 nm. b) Rietveld refinement of the crystal structures found in Ir/ATO catalyst powder. Red crosses are the XRD data obtained, the black line is the calculated diffractogram, and the blue line is the difference between both. The green lines are the Bragg reflections for ATO (upper) and metallic Ir (bottom) phases.

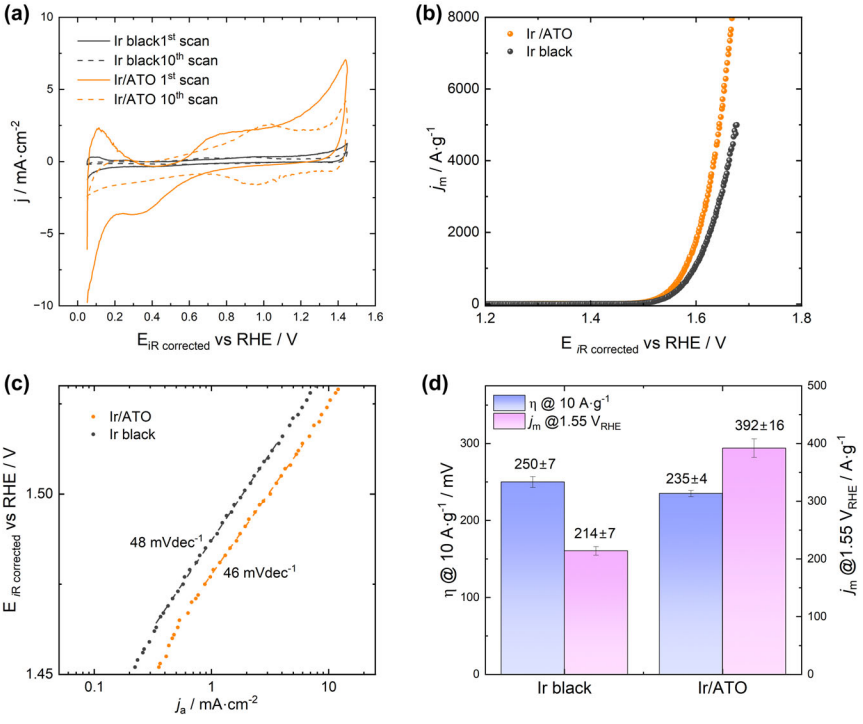

Figure 2. a) Cyclic voltammetry (CV) curves of Ir/ATO (solid orange: initial, dashed orange: after 10 cycles) and Ir black (solid gray: initial, dashed gray: after 10 cycles) for comparison. b) Mass-normalized OER activity for Ir/ATO (orange) and Ir black (gray). c) Tafel slope of Ir/ATO (orange) and Ir black (gray). d) Comparison of catalysts' overpotential at 10 A g^{-1} and mass-normalized current density (j_m) at 1.55 V_{RHE}.

2.2. Oxygen Evolution Reaction Activity

To assess the surface electrochemical properties of as-synthesized Ir/ATO, cyclic voltammetry (CV) was conducted in argon-purged 0.5 M H_2SO_4 solution at a sweeping rate of 50 mV s^{-1} at 2500 rpm with the help of a rotating disk electrode at room temperature. For comparison, commercial Ir black (Umicore) was also evaluated under identical conditions. CV experiments were conducted within a voltage range of 0.05–1.45 V_{RHE}. **Figure 2**a illustrates a voltammogram of the Ir/ATO and Ir black. Both catalysts show a H_{UPD} (hydrogen under potential deposition) peak between 0.1 and 0.2 V_{RHE}. The peak is more pronounced for the Ir/ATO catalyst (Figure S1a, Supporting Information), which resembles the peak observed in the first CV of Ir black (Figure S1b, Supporting Information). This suggests that the nature of dispersed Ir is metallic in as-synthesized Ir/ATO. However, after 10 repetitions, the H_{UPD} has completely vanished, indicating irreversible loss of the metallic character of Ir. Two other broad peaks are also evident between 0.6–0.8 V_{RHE} and ~0.97 V_{RHE}. These peaks are assigned to the formation of Ir(III) and Ir(IV).[33,41]

A long-term CV (Figure S2a, Supporting Information) was performed to understand the evolution of these individual peaks. During the early cycles of CV, the Ir surface undergoes progressive oxidation, at ~0.97 V_{RHE}, forming 3D hydrous IrO_x.[42] After ~50 cycles, the oxidation peak stabilizes (Figure S2c, Supporting Information). This indicates that the surface has reached a steady state where the thickness and structure of the IrO_x layer no longer change significantly. It is also interesting that peaks of the formation of Ir(III) shift positively (between 0.65 and 0.75 V_{RHE}) with each cycle (Figure S2b, Supporting Information). This behavior can be seen where the Ir has been dispersed on Ti_4O_7.[19]

OER activity was determined through linear sweep voltammetry (LSV) between 1.2 and 1.7 V_{RHE} at a scan rate of 10 mV s^{-1}. The second cycle of LSV was taken into account while comparing all the parameters of the catalysts.[30] Figure 2b shows the mass-normalized OER activity of Ir/ATO and Ir black catalysts. It is evident that the as-synthesized catalyst exhibits superior performance over the entire potential range compared to commercial Ir black. This indicates that Ir/ATO more effectively utilizes Ir, due to better dispersion of the Ir on the ATO, which increases the number of active sites exposed to the reaction. To evaluate the reaction kinetics, *i*R-free Tafel plots were determined from fitting of the polarization curves between 1.460 and 1.510 V_{RHE}. In Figure 2c, the Tafel slopes of both catalysts are compared, showing similar values of 48 mV dec^{-1} for Ir/ATO and 46 mV dec^{-1} for Ir black, indicating that both follow similar OER reaction mechanisms.

To quantify the OER activity of the catalyst, the samples were compared at 10 A g_{Ir}^{-1} (Figure 2d) and at 1.55 V_{RHE}. The overpotentials at 10 A g_{Ir}^{-1} for Ir/ATO and the commercial Ir black catalyst were 252 ± 7 and 235 ± 4 mV_{RHE}, respectively. At 1.55 V_{RHE}, the synthesized catalyst shows the mass-normalized current density of 392 ± 16 A g_{Ir}^{-1}, while for Ir black, it is only 214 ± 7 A g_{Ir}^{-1}. The improved

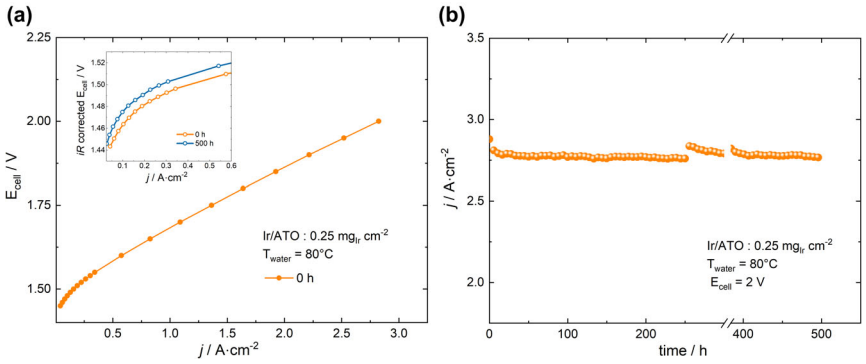

Figure 3. Proton exchange membrane water electrolysis (PEMWE) measurement at 80 °C and ambient pressure with Ir/ATO as anode catalyst (0.25 mg_{Ir} cm^{-2}) and Pt/C as cathode catalyst (0.8 mg_{Pt} cm^{-2}) deposited on a Nafion® N117 membrane. a) Current density with respect to cell potential recorded potentiostatically up to 2 V at 0 and 500 h. (a: inset) Zoomed-in view of *iR*-free polarization curve at 0 and 500 h till ~0.6 A cm^{-2}. b) Evolution of current density over time at constant 2 V with a break in the *x*-axis in between 300 and 384 h.

OER mass activity of the synthesized catalyst may be attributed to the fine dispersion of metallic Ir particles on the support, increasing the number of exposed OER sites. For the primary screening of the longevity of the Ir/ATO catalyst, chronopotentiometry was performed at 10 mA cm^{-2} for 4.5 h (Figure S2d, Supporting Information). A certain gradual increase in the electrode potential is visible for Ir black, while Ir/ATO remains stable throughout the testing duration. Although Ir black was used as the primary reference catalyst in this study, we also evaluated commercial IrO_2 (Alfa Aesar) under identical rotating disk electrode (RDE) conditions to provide a state-of-the-art (SoA) benchmark. The results (Figure S4, Supporting Information) show that Ir/ATO outperforms IrO_2 across all key metrics, including 11 mV lower overpotential at 10 and 115 A g_{Ir}^{-1} higher mass activity at 1.55 V_{RHE}. This reinforces that the superior performance of Ir/ATO is not only evident when compared to Ir black but also holds against the widely accepted benchmark IrO_2.

2.3. PEMWE Cell Performance and Durability

The performance of the Ir/ATO anode catalyst was evaluated in a PEMWE cell at a catalyst layer loading of 0.20 mg_{Ir} cm^{-2}. Additionally, the anode PTL is sputter-coated with ~0.1 mg_{Ir} cm^{-2}, taking both the facets into account. However, only the interface in direct contact with the catalyst layer can effectively contribute to the OER due to the requirement of ionomer contact for establishing the triple-phase boundary. Taking this into account, the effective Ir loading is reasonably estimated as ~0.25 mg_{Ir} cm^{-2}. The cell was operated at a water temperature of 80 °C and ambient pressure. Complete single-cell configurations and testing conditions are listed in Table S2, Supporting Information. At the beginning of the test, this cell delivered a current density of ~2.82 A cm^{-2} at 2.0 V (**Figure 3a**), corresponding to ~63% efficiency (LHV). Such performance is comparable to SoA PEMWE cells that employ significantly higher Ir loadings, and it falls within the range of other reported PEMWE results using Ir supported on ATO (Table S3, Supporting Information). To ensure reproducibility of cell performance, three independent PEM single cells were assembled employing Ir/ATO, and polarization curves were recorded under identical operating conditions (Figure S5, Supporting Information). The current density at 2.0 V varied within the narrow range of 2.75–2.87 A cm^{-2}, corresponding to a standard deviation of <2.5% (2.815 ± 0.05 A cm^{-2}) and a standard error of <1.5% (2.815 ± 0.036 A cm^{-2}), thereby confirming the robustness and reliability of the reported performance data. For direct comparison with a SoA reference catalyst, a PEMWE cell employing commercial IrO_2 at 2 mg_{Ir} cm^{-2} was also tested under identical conditions. As shown in Figure S6, Supporting Information, IrO_2 delivered ~2.74 A cm^{-2} at 2.0 V, whereas Ir/ATO achieved ~2.82 A cm^{-2} at the same cell voltage despite a tenfold lower Ir loading. This confirms that Ir/ATO not only matches the SoA reference performance but does so with reduced Ir content, underlining its high catalyst utilization efficiency. While these initial metrics indicate that the Ir/ATO electrode can reach high performance comparable to SoA configurations, initial performance alone does not guarantee stability of the electrode. To study the degradation mechanisms of the Ir/ATO electrode, a 500 h durability test was carried out.

The PEMWE cell was operated at a constant voltage of 2 V (Figure 3b), with polarization and electrochemical impedance spectroscopy (EIS) measurements recorded over time. A gradual, although minimal, decline in current density was observed throughout the test. Over the first 125 h, a performance loss of 0.70% (3.51 mA h^{-1}) was recorded, followed by a continued but slower decline over the next phase of operation (between 125 h and 225 h; 0.25% or 1.14 mA h^{-1}). By the final measured interval between 400 and 500 h, the degradation rate increased again to 0.67% (3.33 mA h^{-1}), comparable to the initial phase. While variations in degradation rates were observed across different time intervals, the overall trend indicates a steady loss in performance over 500 h of operation (see Table S4, Supporting Information).

EIS measurements were conducted to clearly separate electrode kinetics and changes in cell resistance during PEMWE operation. The *iR*-corrected polarization curves after 500 h (inset Figure 3a and Figure S7c, Supporting Information) showed a clear upward shift in cell voltage at all current densities, particularly at low current densities (<0.6 A cm^{-2}; Figure S7d, Supporting Information), a region dominated by OER kinetics, highlighting degradation in anodic catalytic activity and increased overpotential. Concurrently, a clear reduction in high-frequency resistance (HFR) (Figure S7b, Supporting Information) was observed after operation, indicating lower ohmic resistance in the PEMWE cell. This behavior is observed by many researchers[43–45] and primarily attributed to prolonged exposure of the membrane to operational humidity levels, which enlarges ionic conducting structures like channels within the membrane, thus reducing resistance over time.[46] Improved PTL and catalyst ACL contact may also contribute to reduced ohmic resistance.[47] Lettenmeier et al.[46] have first reported this phenomenon during extended PEMWE operation at high current densities. Despite detecting a loss of ionomer and iridium through postmortem physicochemical analyses, they reported an overall *apparent* performance improvement of PEMWEs primarily due to a significant reduction in HFR. This study highlights how such HFR decreases can partially obscure underlying degradation mechanisms by masking real cell behavior. Though we observed only minimal degradation in our study,

it remains crucial to fully uncover the underlying catalyst degradation mechanisms of Ir/ATO to understand its long-term impact on PEMWE performance.

2.4. Morphology and Surface Properties of Anode Catalyst Layer

Figure 4 shows the SEM images of the pristine and operated ACLs at different magnifications, providing insights into the morphological changes that occur post-operation. In the pristine state (Figure 4a–c), the ACL exhibits a relatively smooth, uniform surface with a fine distribution of nanoparticles, where Ir (brighter area) particles are distributed on top of grayish ATO support, characteristic of freshly prepared catalyst layers. At these higher magnifications, the images reveal a porous structure. The pore sizes are small, well-defined, and uniformly distributed, indicating a structure capable of two-phase flow, promoting effective ion and gas transport while eliminating localized electrochemical reactions.

However, after 500 h of operation, the SEM images of the ACL reveal significant morphological changes which are evident looking at the low magnification SEM images (Figure S8, Supporting Information). The top view of the operated ACL shows the imprint of the PTL (Bekaert Ti felt), which is visible as a series of crests and grooves originating from the clamping compression during cell assembly. Figure 4d–f shows that the operated ACL exhibits a rougher surface with a reduced number of smaller pores, while a few larger pores dominate the structure. Figure S13, Supporting Information, shows the comparison of pristine and operated ACL measured with high-resolution atomic force microscopy (AFM) tip, showing the same phenomenon of increased number of large pores and reduced smaller pores. This change suggests structural reorganization of the ACL during operation. The uneven pore distribution, along with the presence of larger voids and clustering, likely reduces the total catalytic surface area, contributing to a decline in PEMWE stability, particularly in the OER-controlled region. This observation aligns with the iR-free polarization curves (Figure S7c,d, Supporting Information), which reveal a decrease in OER catalytic activity.

Figure 5 provides cross-sectional SEM images of both the pristine and operated ACLs, along with EDX mappings to analyze the elemental distribution of Ir and fluorine (F). In the pristine state (Figure 5a), the ACL shows a smooth and uniform structure with well-defined thickness. High-resolution images can be seen in Figure S9a,b, Supporting Information. The particles are evenly distributed within the catalyst layer, tightly packed, and free from large voids, indicating strong bonding to the underlying polymer membrane. This bonding ensures mechanical integrity and minimal risk of delamination during operation. Similar to before, imprints of the PTL can be seen in Figure S10b, c, Supporting Information. Importantly, Figure 5b highlights the robustness of the ACL under mechanical compression in the contact region with PTL. No cracks were observed at the interface between regions of the catalyst layer compressed under the PTL and adjacent regions that remain uncompressed. The global catalyst layer thickness also seems to be preserved. Notably, the PTL applies localized pressure on the catalyst layer at points of contact. Rather than pushing into the layer itself, it compresses the membrane underneath, causing a local reduction in membrane thickness. The cross-sectional images also show that the catalyst layer is partially embedded into the membrane (Figure S10d, Supporting Information) at localized areas; a phenomenon that happens when the pristine catalyst layer is hot pressed before

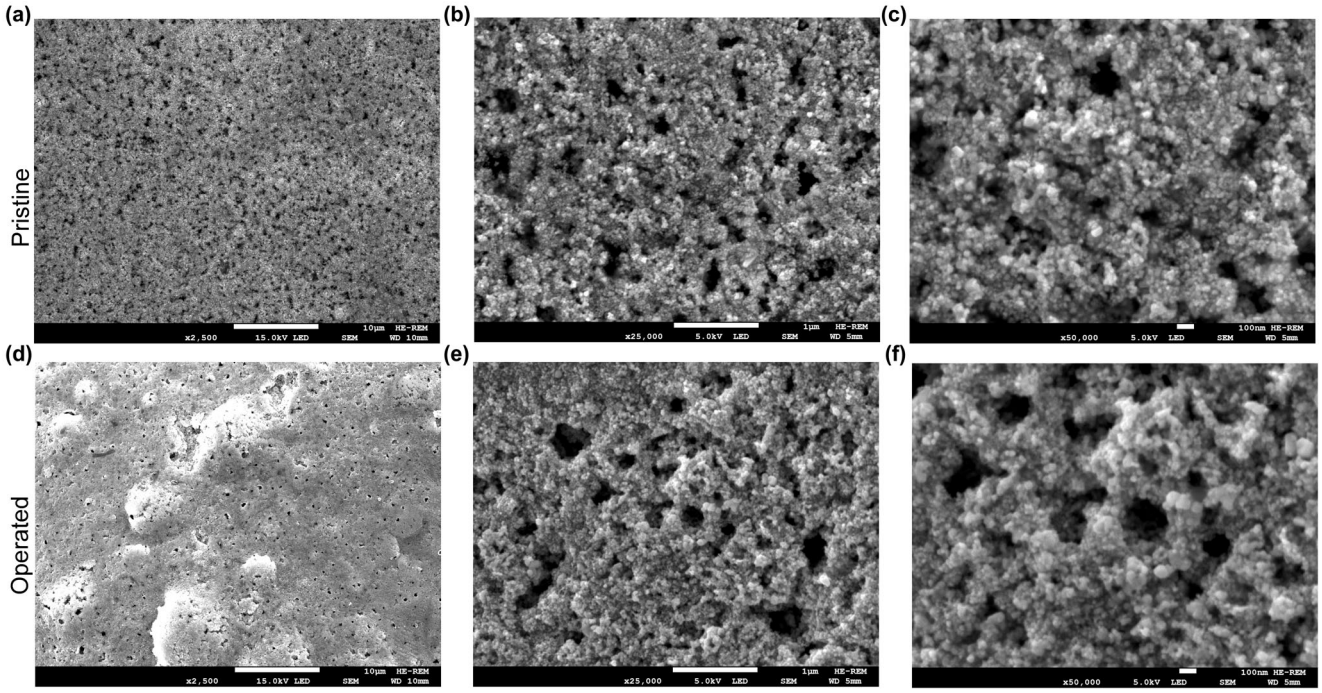

Figure 4. Pristine and operated anode catalyst layer surface characterization with scanning electron microscope (SEM). Pristine anode catalyst layer (on-top view) with different magnification a) 2500× b) 25 000× and c) 50 000× with scale bar representing 10 µm (a), 1 µm (b), and 100 nm (c). Operated anode catalyst layer (on-top view) with different magnifications, d) 2500×, e) 25 000×, and f) 50 000× with scale bar representing 10 µm (d), 1 µm (e), and 100 nm (f).

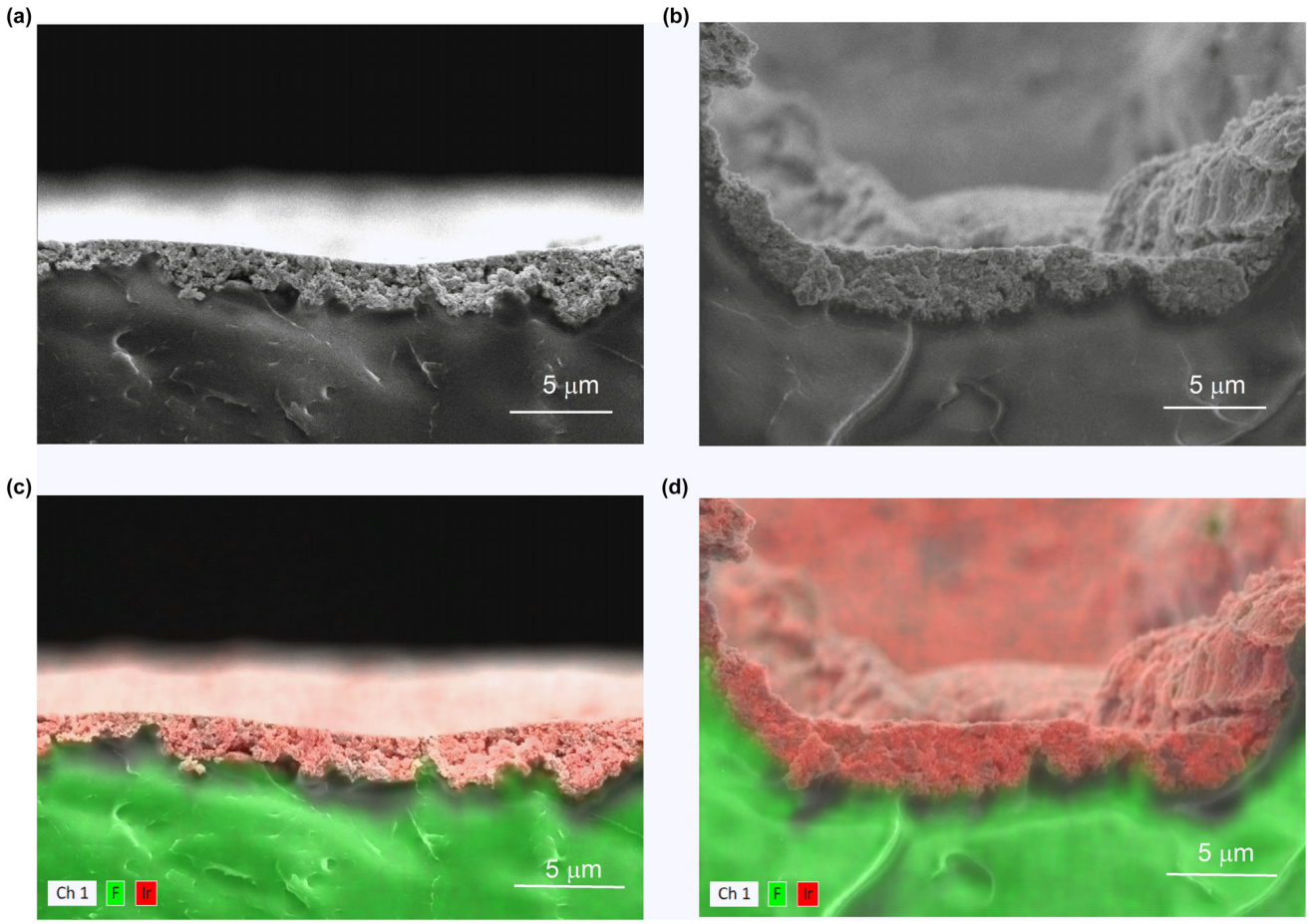

Figure 5. Cross-section SEM image of a) pristine and b) operated anode catalyst layer at 5000× magnification with white scale bar representing 5 µm EDX images of c) pristine and d) operated anode catalyst layer with red area and green area representing Ir and fluorine (F) signal.

application in PEMWE. At the larger imprint area in Figure 5b some larger particles were observed at the membrane/ACL interface that may have been formed during operation or are embedded, as described above, due to the applied pressure. Notably, these particles have not migrated in the membrane and stayed at the interface.

Nevertheless, minuscule and discrete Ir dissolution and redeposition into the membrane cannot be ruled out in localized areas, as the spatial resolution of SEM is insufficient to unambiguously detect discontinuous or incipient low concentration Ir band formation at the membranes/ACL interface.[48] The elemental mapping of the cross-section of ACL (Table S5, Supporting Information) corresponding to Figure 5c,d shows no notable change in the Ir distribution in ACL after operation. Nevertheless, EDX evaluation of the cross-section was conducted at 5 kV due to the rapid damage observed in the membrane at 15 kV. As a result, the measurements of Sn and Sb may lack precision at the lower accelerating voltage. Most importantly, there is no continuous visible Ir band within the membrane, which implies little dissolution, migration and reposition of Ir within the membrane, which is in contrast to some PEMWEs where unsupported Ir is used.[46,49]

Figure 6 presents AFM measurements, including topography, tunneling atomic force microscopy (TUNA) current, average current during force separation curve, and Derjaguin-Muller-Toporov (DMT) modulus, for pristine and operated ACLs. These measurements were conducted over a 25 μm^2 area. AFM height measurements reveal significant changes in surface roughness after operation. The pristine ACL (Figure 6a) exhibits a relatively smooth surface with minor irregularities and limited height variation, indicative of a uniform surface structure. The average roughness (R_a) of the pristine ACL is measured at 18 nm, while it is 43 nm for the operated ACL (Figure 6d) with $R_{max} \sim 651$ nm, indicating the development of crests and valleys. This observation is similar to the one obtained for SEM images. TUNA current measurements, performed at 1 V bias, provide insights into the conductive area of the ACL. For pristine ACL (Figure 6b), 39% of the measured area is electrically conductive. However, in operated ACL (Figure 6e), the electrically conductive area increases significantly to 58.5%. This increase suggests that catalyst particles in contact with the PTL are either no longer covered by ionomer or are covered by a thinner ionomer layer, enabling higher electron conduction.[50] Liu et al.[51] have observed a similar increase in conductivity at the interface of ACL and PTL while using IrO_2 catalyst. However, this localized degradation/redistribution of ionomer at the ACL/PTL interface may leave some Ir particles unutilized due to the lack of proton-conducting media, potentially reducing catalytic performance. This effect is evident in the iR-free polarization curves, particularly in the OER-controlled region (Figure S7c,d, Supporting Information). In addition, such degradation would not only hinder ionic conductivity but also make the ACL

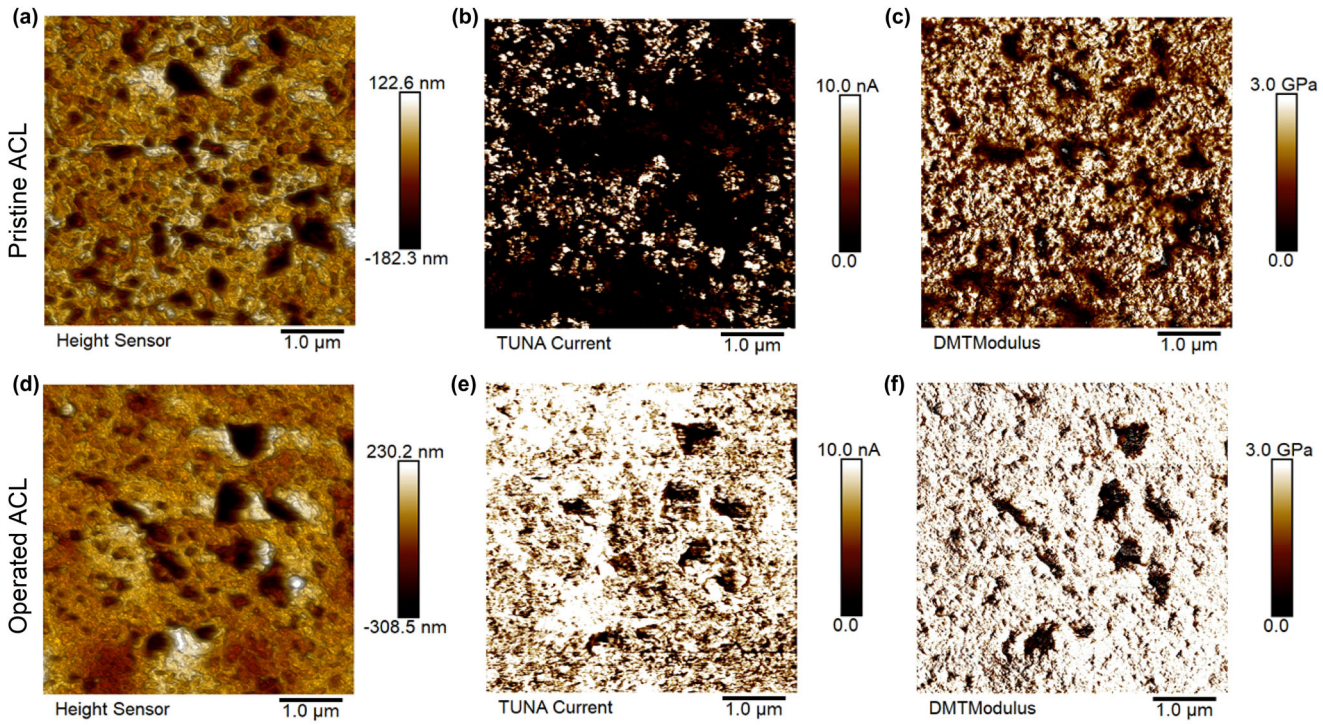

Figure 6. Atomic force microscopy measurement for topography, TUNA current, and Derjaguin-Muller-Toporov (DMT) modulus of pristine (a, b, c) and operated (d, e, f) anode catalyst layer.

more prone to delamination over time, posing a risk to long-term cell stability. Additional images with V(i) curves at each measurement point are shown in Figure S11, Supporting Information, for pristine and operated samples, revealing the increased conductivity after operation. On both sets of images, an ionomer-covered area, with no electronic conductivity, is present in the middle of the sample. Figures S12 and S13, Supporting Information, reveal the surface structure of the pristine and operated anode measured with a super sharp AFM tip at different resolutions. Further evidence of ionomer redistribution or thinning in the operated ACL can be inferred from the DMT modulus measurements, which provide a measure of surface stiffness. Here, pristine ACL (Figure 6c) exhibits lower stiffness, consistent with a thicker ionomer layer providing mechanical flexibility. In contrast, the operated ACL (Figure 6f) displays a marked increase in stiffness, indicative of reduced ionomer thickness or partial ionomer degradation. These changes in mechanical properties align with the observed topographical and conductive changes, further supporting the ionomer degradation during extended operation.

2.5. Structure, Morphology, and Surface Properties of Ir/ATO Catalyst

XRD pattern of powder and operated catalyst is shown in **Figure 7**. In both cases, broad reflections at approximately 40.5°, 46.5°, and 69° are observed, giving the initial impression that the Ir nanoparticles might remain metallic in nature after extended operation. We evaluated the changes in the crystal size of Ir and ATO before and after the PEMWE operation. The initial catalyst presents a D_{ATO} of 18 nm (±3 nm) and D_{Ir} of 3 nm (±1 nm). The operated catalyst has a D_{ATO} of 12 nm (±3 nm) and $D_{Ir\ phase}$ of 2 nm (±1 nm). Therefore, the size of ATO crystals is decreasing, while for the Ir phase, it remains similar. However, this interpretation must be treated with great caution, since the operated catalyst XRD was measured on a catalyst-coated membrane; it is important to note that reflections corresponding to metallic Pt, originating from the cathode side, occur at diffraction angles very similar to those of metallic Ir (see lower part of Figure 7). In addition, broad reflections corresponding to carbon (from ionomer and membrane) can be observed in the operated catalyst. Furthermore, the characteristic low-index reflections of IrO_2 (110, 101) overlap with those of ATO, making it challenging to draw a definitive conclusion about the state of Ir nanoparticles based solely on the XRD data.

To further probe the differences found in the ATO support and the Ir phase between the initial powder catalyst and the operated one in terms of size, morphology, distribution, and composition, we performed transition electron microscopy (TEM). **Figure 8**a shows that the powder catalyst is composed of ATO with an average size of 23 nm (±11 nm) and metallic Ir averaging 1.8 nm (±0.5 nm). The crystalline nature of ATO is evident from its distinct lattice planes and its SAED, as shown in Figure 8b. Furthermore, the high-resolution images (Figure 8c,d) show that the small Ir nanoparticles are crystalline in nature rather than amorphous, displaying well-defined crystallographic planes that likely correspond to metallic Ir, with interplanar distances of 2.2 Å, which corresponds to the (111) crystal plane of Ir in the Fm3m space group. The powder catalyst exhibits a typical morphology of a *bunch of grapes* of the Ir nanoparticles aggregated on the surface of the larger ATO particles. Elemental composition determined by EDX shows that the smaller nanoparticles are solely composed of Ir, while the larger

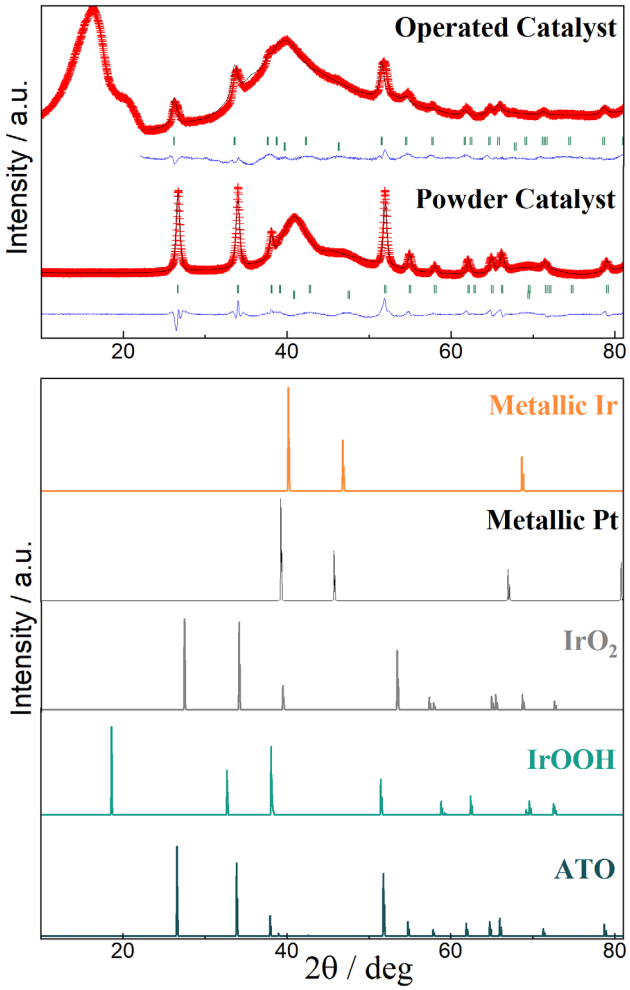

Figure 7. Rietveld refinement of the crystal structures using X-ray diffraction patterns of the powder catalyst and the operated catalyst. The calculated X-ray patterns of the most relevant phases are shown in the lower panel.

ATO particles have the stoichiometry of $Sb_{0.10\pm0.03}Sn_{0.90\pm0.03}O_x$. After the PEMWE operation, TEM images (Figure 8e) reveal noticeable morphological changes in the operated catalyst. The average size of ATO has decreased from 23 nm (±11 nm) to 14 nm (±9 nm). In contrast, the Ir particle size remains similar to the initial powder sample at 1.7 nm (±0.4 nm). Also, the particles show a crystalline structure even after prolonged operation (Figure 8f–h). The crystalline phases have interplanar distances again close to 2.2 Å, which may be ascribed to (111) crystal planes of metallic Ir; but are also close to (011) and (002) of IrOOH at around 2.3 Å, and (111) of IrO_2 at 2.2 Å. In addition, we also observed an interplanar spacing of approximately 3.3 Å at regions where both nanoparticles and larger crystals coexist. This distance could correspond to the (110) planes of IrO_2 (3.2 Å), but it is also consistent with the (110) planes of ATO (3.4 Å), which is the most frequently observed spacing in ATO (Figure 8f). Therefore, for better clarity about the nature of the Ir species, XPS and XAS studies are also performed. TEM also shows that the migration and agglomeration of Ir nanoparticles are inhibited on the surface of ATO particles, which is an indication of a strong metal-support interaction (SMSI). Notably, the operated catalyst shows Ir particles embedded in a matrix (Figure 8g), possibly a carbon-containing layer derived from the ionomer that could facilitate better dispersion of the Ir nanoparticles throughout the catalyst layer. Siracussano et al.[52] have observed a similar phenomenon in operated catalyst morphology and attribute such dispersion to oxygen evolution within particle agglomerates or ionomer infiltration. EDX analysis of the operated catalyst indicates a decrease in Sb content from 10 wt.% to 4 wt.%, showing the leaching of Sb during PEMWE operation. Our results are in good agreement with the previous studies carried out with a similar catalyst in a half-cell, in which Sb_2O_5 dissolution was proposed at anodic potential exceeding 1.1 V_{RHE}.[36] and cycling between 0.4 and 1.0 V_{RHE}.[53] We also have observed a significant reduction in the size of ATO. This might be due to the operation of PEMWE at an iR-free cell voltage of 1.55 V for extended periods, which is well above the potentials of 1.45 V_{RHE} required for electrochemical dissolution of SnO_2 determined in half-cell studies. Although the dissolution of Sb and Sn oxides does not immediately result in catastrophic PEMWE performance loss in our experiments, over extended operation, it can lead to the gradual detachment of Ir particles from the support, reducing the amount of active Ir available for catalysis. Identifying this early sign of support instability is crucial for understanding the long-term durability of the catalyst.

Moreover, the surface nature of the Ir was analyzed by X-ray photoelectron spectroscopy (XPS), as shown in **Figure 9**. The evolution of the Ir oxidation state was assessed by comparing the deconvoluted 4f spectra of powder and operated anode catalysts. The spectra were deconvoluted using a Shirley background and asymmetric line shapes for the Ir 4f region. The XPS spectrum of the powder catalyst (Figure 9a) reveals a characteristic Ir 4f doublet with the Ir 4f7/2 peak centered at 60.37 eV and a spin-orbit splitting of approximately 3 eV. This binding energy (BE) corresponds to metallic Ir (Ir^0) species.[54,55] Along with the main 4f peaks, some studies report the presence of smaller peaks at lower binding energies, ascribed to surface core level shifts.[55] However, this peak is not usually observed when using conventional laboratory sources.[54]

The BE of the operated sample (Figure 9b) showed a significant shift of the Ir 4f doublet to higher binding energies. The Ir $4f_{7/2}$ peak is centered at 62.29 eV, accompanied by two low-intensity satellite peaks approximately at 1 eV higher binding energies than the primary $4f_{7/2}$ and $4f_{5/2}$ peaks. This increase in BE suggests a transition from metallic Ir (Ir^0) to higher oxidation states, with the surface being dominated by hydrous Ir oxide species such as hydrated IrO_2 or hydrous IrO_x species present in the +3 oxidation state[52,56,57] These findings highlight the surface transformation of Ir during operation, where the pristine metallic state (Ir^0) of the powder catalyst transitions to oxidized forms ($IrO_x{\cdot}OH_y$) in the operated catalyst layer.

To better study the nature of the Ir species after operation, an XAS study was performed to probe the Ir L_3-edge of the catalyst. Spectra were collected at the CLAESS beamline of ALBA synchrotron using a Si 311 double crystal monochromator operating in continuous mode. The collimating mirror with Rh coating was used to attenuate the highest harmonics. The beam size of 200 × 300 µm (H × V) was used. All spectra were collected in transmission mode. The XANES region in the powder catalyst has spectral features present as in the metallic Ir, but with a more intense white line (**Figure 10a**). The operated catalyst is similar to IrO_2, but also has a more intense first peak. This effect can be attributed to changes in the unoccupied 5d states caused by strong metal-support interactions, making the electronic structure different from that of bulk Ir standards. The FT-EXAFS (Figure 10b) shows the presence of an Ir-Ir peak around 2 Å for the initial powder sample.

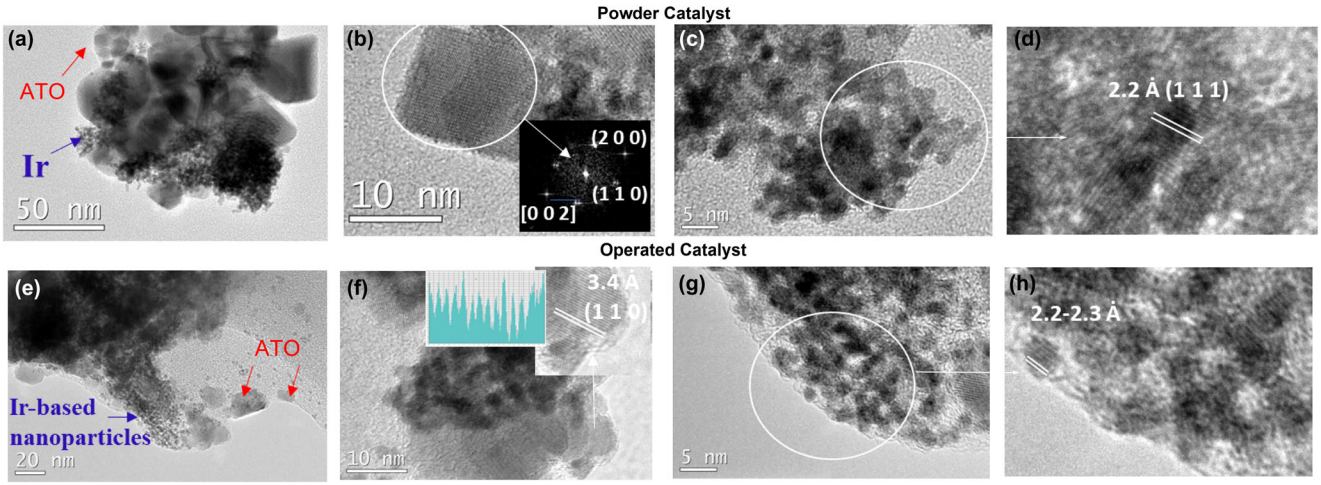

Figure 8. Transition electron microscopy (TEM) micrograph of powder catalyst (a–d). TEM and high-resolution transition electron microscopy (HRTEM) micrographs of the operated anode catalyst scratched from the anode catalyst layer (e–h).

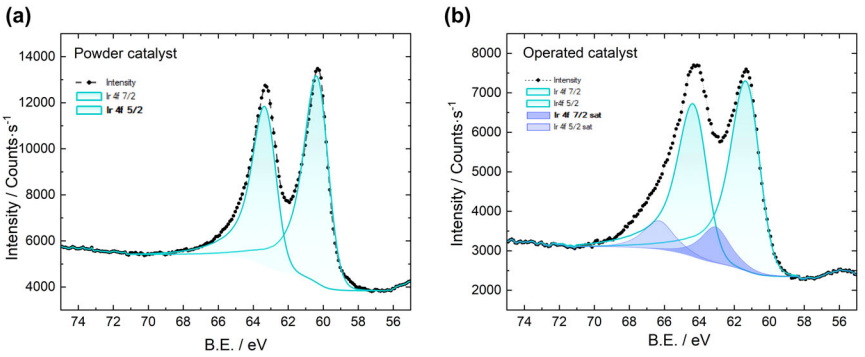

Figure 9. X-ray photoelectron spectroscopy (XPS) spectrum showing the Ir 4f region of a) the powder catalyst and b) the operated catalyst from the anode catalyst layer.

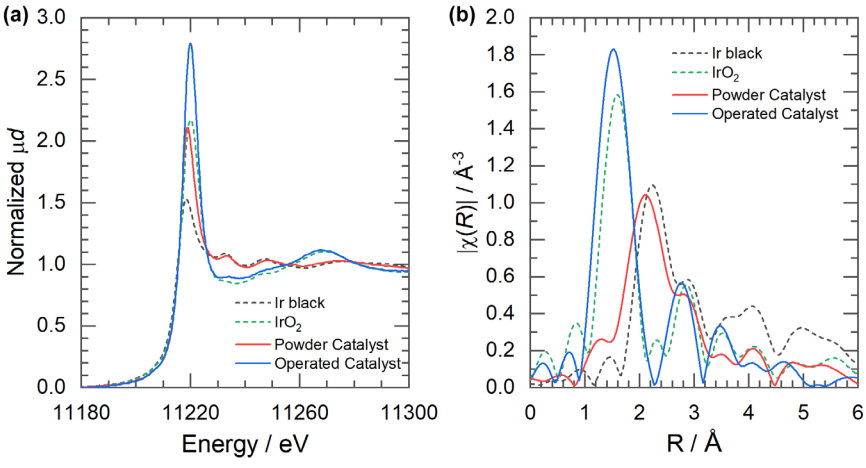

Figure 10. Ir L_3-edge XANES spectra (a) and respective FT-EXAFS (b) of powder catalyst (solid red), operated catalyst (solid blue), IrO_2 (dashed green), and Ir black (dashed brown) standards.

Surprisingly, the operated catalyst does not contain a distinguishable peak related to the Ir-Ir metal bond, while the Ir-O peak appears at around 1.5 Å. That indicates that the operated catalyst is not metallic Ir but has an oxidized phase of Ir, probably related to $IrO_x{\cdot}OH_y$. Consistently, complementary XAS measurements at the Pt L_3-edge revealed that Pt remains metallic after operation (Figure S14b, Supporting Information), whereas Ir undergoes oxidation. This indicates that the broad fcc-type reflections in XRD measurements originate from Pt particles only, while Ir exists as oxide clusters. It should be noted that in both samples, the interatomic distance (Ir-Ir on the powder sample and Ir-O in the operated one) is slightly contracted. Quantitative analysis of EXAFS spectra is limited due to the presence of Pt in the operated catalyst-coated membrane (CCM), which significantly shortened the signal in k space.

3. Conclusion

This study provides an in-depth investigation into the degradation phenomena of low-loaded Ir/ATO-based anodes in PEMWE operated under realistic conditions. Despite operating at high current densities and extended durations, no continuous Ir band formation was observed within the membrane, unlike unsupported Ir catalysts that show extensive Ir migration.[46,49,58] This indicates suppressed Ir dissolution and redeposition, although smaller localized Ir migration and redeposition cannot be entirely excluded. Morphological analyses (SEM, TEM) further confirmed the preservation

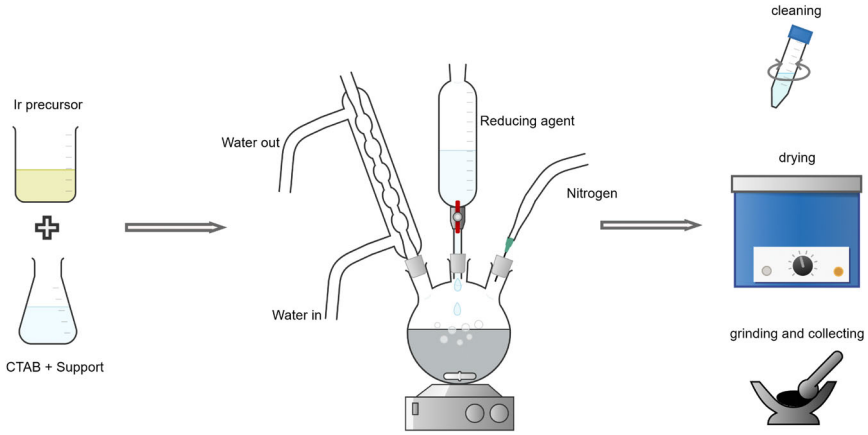

Figure 11. Schematics of the synthesis process of Ir/ATO.

of Ir-based nanoparticle size (~1.7–1.8 nm), indicating that ATO anchors Ir nanoparticles effectively and prevents their bulk agglomeration, electrochemical dissolution, and transport. In agreement with the trends reported by Oh et al.,[29] the observed stabilization behavior may suggest the presence of SMSI between Ir and ATO. This is further corroborated by our XAS analysis, where the intensified white line in the pristine catalyst and the evolution toward dominant Ir–O coordination upon operation both point to SMSI influencing the electronic structure of Ir in contact with ATO. Though oxidized, Ir nanoparticles retained their size, while partial ATO degradation was evident. The observed leaching of Sb and Sn suggests that, despite ATO effectively inhibiting Ir dissolution, it exhibits chemical instability under OER conditions. Dissolution of support should be viewed as an early symptom that the long-term catalytic durability may be compromised by changes in the surrounding matrix. Interestingly, despite Ir-based nanoparticle size stability, an increase in activation overpotential was observed in the *i*R-free polarization curves. This reduction in electrochemical performance is attributed to the ionomer degradation at the ACL/PTL interface (confirmed by AFM studies), which limits proton access to active Ir sites, leaving them catalytically unutilized. SEM and AFM analyses further revealed morphological restructuring at the ACL/PTL interface, indicating a shift toward larger pores. This structural reorganization likely reduces the effective catalytic surface area, further contributing to performance degradation in OER kinetics-limited regions.

These insights offer a foundation for designing next-generation anodes that combine ultra-low-Ir content with structurally resilient interfaces, accelerating the path toward economically viable green hydrogen production.

4. Experimental Section

Catalyst preparation: The deposition of Ir onto the as-received ATO (NanoArc®, Thermo Fisher) was achieved based on a previously established wet chemical synthesis method (**Figure 11**).[59] Initially, 1.17 g of $IrCl_3 \cdot xH_2O$ was dissolved in 350 mL of absolute ethanol (Merck Millipore®) to form a precursor solution. In parallel, 715 mg of as-received ATO powder was dispersed in an equal volume of absolute ethanol, ensuring homogeneity through ultrasonication. These two solutions were then combined, and 13.8 g of cetyltrimethylammonium bromide (CTAB, VWR Chemicals) was added to optimize and control Ir size at the nanometer scale. The reduction solution was prepared by dissolving 7.18 g of $NaBH_4$ (VWR Chemicals) in 120 mL of absolute ethanol. The reduction process was initiated by introducing a reduction solution dropwise under a nitrogen (N_2) atmosphere, with continuous stirring to promote uniform reduction. The reaction mixture was allowed to stir overnight, ensuring full reduction of the Ir precursor. Following the reaction, the catalyst was extensively rinsed with ultrapure water and ethanol to remove any residual byproducts. The resultant Ir/ATO catalyst was dried in an oven at 60 °C for 12 h, then ground to a fine powder for further electrochemical testing.

Physicochemical characterization: SEM measurements were performed using a JEOL field emission microscope (JSM-7200F) equipped with a Schottky Emitter. Samples measuring approximately $0.5 \times 0.5\ cm^2$ were extracted from the CCM using a razor blade for both pre- and post-operation measurements. Each sample was fixed to the SEM sample holder with double-sided carbon tape to ensure stable positioning during imaging. A working distance of 10 mm and 5 or 15 kV accelerating voltage were used for the measurements. To explore the inner parts of the sample's cleavage, liquid N_2 was used. The samples were kept for at least 5 min in liquid N_2 and cleaved directly in liquid N_2. The cleaved samples were observed with 5 kV accelerating voltage using an E-T secondary electron detector. EDX was performed with a Bruker Quantax detector using 5 and 15 kV accelerating voltage when needed for the detection of the elements. The powder samples were analyzed with a Zeiss crossbeam 350 FE-SEM using E-T secondary electron and energy-selective backscattered detectors.

AFM measurements were performed with Icon XR AFM (Bruker Nano Surfaces Inc., Karlsruhe, Baden-Württemberg, Germany) in PeakForce-TUNA mode with PPP-NCHPt tips (Nanosensors) using a 1 V bias and in PeakForce QNM mode using super sharp silicone (SSS-FMR) tips (Nanosensors). Small samples were attached to 12 mm magnetic AFM steel discs with conductive tape, which was also placed on top of the catalyst layer close to the measurement area. In addition, DCUB-TUNA (Bruker) V(i) measurements were performed using DDESP diamond-coated tips.

XRD was used to identify the phases present on each sample. A Bragg–Brentano reflection geometry with CuK_α radiation ($\lambda = 1.5418$ Å) was used. To refine the crystal structures and estimate the size of the coherently diffracting crystalline domains, we employed the Rietveld method using the FullProf Suite.[60] The crystal sizes are measured by using the Scherrer equation with the XRD data (note that this method estimates the size of the coherently diffracting crystalline domains): $D = \frac{k\lambda}{\beta_{size}\cos\theta}$; where D is the average crystalline domain size, k is the Scherrer constant (typically ≈ 0.94), λ is the X-ray wavelength, θ is the Bragg diffraction angle, and β_{size} is the full width at half maximum calculated with the Rietveld refinement method. Transmission electron microscopy (TEM), high-resolution electron microscopy (HRTEM), and X-ray energy-dispersive spectra were obtained using a JEOL 2100 field-emission gun transmission electron microscope, operating at 200 kV, and equipped with a microanalysis system with XEDS (OXFORD INCA).

XPS were acquired using a SPECS GmbH system equipped with an ultra-high vacuum system. The setup included a PHOIBOS 150 9MCD energy analyzer and a non-monochromatic X-ray Mg Kα source ($h\nu = 1253.6$ eV, operating at 200 W/12 kV), an electron source for charge compensation, a UV photon source, an ion source, and a sample pretreatment chamber (HPC). The energy regions of the photoelectrons of interest were scanned at increments of 0.1 eV and a fixed pass energy of 20 eV. The XPS peaks were fitted using Voigt functions (70% Gaussian and 30% Lorentzian) and asymmetric lines on the CasaXPS software.

X-ray absorption spectroscopy (XAS) measurements were performed at the CLÆSS beamline[61] of the ALBA synchrotron. The Ir L-edge XAS spectra were collected in transmission mode using a Si 311 monochromator. The influence of the highest harmonics was rejected by the selection of the respective coating on the collimator mirror. The set of standards was prepared as a pallet and measured in the transition regime. Several scans were acquired to ensure reproducibility and a good signal-to-noise ratio. The data were treated with the Demeter[62] package including calibration and normalization.

Half-cell electrochemical characterization: CV and LSV measurements of the Ir/ATO catalyst powder were performed in a conventional three-electrode electrochemical cell using a RDE configuration (RRDE-3A, BAS Inc., Japan) with an interface 5000E potentiostat/galvanostat (GAMRY instruments). The measurements were conducted at ambient temperature in an argon-purged 0.5 M H_2SO_4 electrolyte. A platinum (or Pt) wire served as the counter electrode, while a reversible hydrogen electrode (Hydroflex, GASKATEL) acted as the reference. The working electrode consisted of a glassy carbon electrode (0.1256 cm^2) coated with a thin catalyst layer. To prepare the catalyst ink, the catalyst powder was dispersed in a 1:3 (v/v) solution of 1-propanol (>99.5%, Sigma Aldrich) and ultrapure water. A 5 wt.% Nafion® D-520 dispersion was added to achieve an ionomer-to-catalyst ratio of 0.2, and the resulting mixture was sonicated for 30 min in an ultrasonic bath (RK 510, BANDELIN electronic GmbH & Co. KG) to ensure thorough homogenization. This ink was then pipetted onto the glassy carbon electrode and dried under the stream of N_2 to achieve an Ir loading of 7.7 μg_{Ir}.

The CV measurements were performed by cycling the potential between 0.05 and 1.45 V_{RHE} for 10 cycles at a scan rate of 50 mV s^{-1}, with the electrode rotating at 2500 rpm. For OER catalytic performance, 5 LSV measurements were conducted by sweeping the potential from 1.2 to 1.7 V_{RHE}. In situ ohmic resistance corrections were performed for all CV and LSV measurements using the potentiostat software to ensure accurate evaluation. Commercial Ir black (Umicore AG & Co. KG) served as the benchmark catalyst for performance comparison.

Catalyst-coated membrane (CCM) preparation: A conventional three-layer CCM was prepared, achieving an Ir loading of 0.2 mg_{Ir} cm^{-2}. The ACL was fabricated using a precision spray-coating system (ExactaCoat, Sono-Tek), with the catalytic dispersions formulated by mixing catalyst powder in a blend of Nafion® ionomer (D1021, Ion Power Inc.), deionized (DI) water, and n-propanol (Merck), cooled in an ice bath, followed by homogenizing with an ultrasonic horn for 30 min. This carefully prepared dispersion was then sprayed onto a Nafion® 117. The membrane was fixed on a heated vacuum plate (90 °C) and immersed in ultrapure water afterwards.

In contrast, the cathode layer was applied using a doctor-blade method (Coatmaster 510, Erichsen GmbH & Co. KG). The cathodic catalyst dispersion comprises mixing 60% Pt/C (FC Catalyst), Nafion® ionomer (LQ1115, Ion Power Inc.), DI water, and 2-butanol (Merck). This mixture underwent high shear blending (Ultra-Turrax, IKA) and subsequent ultrasonic homogenization (Sonopuls HD3400, Bandelin) to ensure a fine and consistent particle distribution. The final cathode layer was adjusted to a catalyst loading of 0.8 mg_{Pt} cm^{-2}. In terms of composition, the cathode catalyst layer contained 20 wt.% Nafion®, while a slightly lower Nafion® content of 11 wt.% was selected for the anode. The cathode catalyst layer (active area 17.64 cm^2) was carefully aligned and transferred onto a Nafion® membrane (N117, Chemours) using a hot-pressing procedure. This process was conducted at a temperature of 130 °C, with a 13 min heat-up and 3 min pressurization of 1.6 kN cm^{-2}.

PEMWE measurements: The single-cell tests were performed in an in-house-designed cell and test station[63] with an active cell area of 17.64 cm^2 (Ir/ATO) and 25 cm^2 (IrO_2) at 80 °C at ambient pressure. Bekipor® ST titanium grade 1 felts with a thickness of 350 µm and 56% porosity from Bekaert (42 × 42 mm), with a noble metal (Ir) coating of 0.05 mg_{Ir} cm^{-2} on either facet[64] were used as the anodic PTL. TGP-H 120 Toray paper with a thickness of 350 µm was used as the cathodic PTL. The break-in procedure for the PEMWE can be found in the literature.[63] AC impedance measurements were performed between 100 mHz and 10 kHz using a current perturbation between ±5% of cell current. EIS measurements were performed at every voltage step at 0, 250, and 500 h. The HFR was determined from the high-frequency intercept of the Nyquist plot with the real axis.

Acknowledgements

The authors acknowledge the PROMET-H2 project. This project has received funding from the European Union's Horizon 2020 research and innovation program under grant agreement No 862253. MR and SR also acknowledge the Spanish grant TED2021-131033B-I00 from MCIN/AEI/10.13039/501100011033. Open Access funding enabled and organized by Projekt DEAL.

Conflict of Interest

The authors declare no conflict of interest.

Supporting Information

Supporting Information is available from the Wiley Online Library or from the author.

Keywords

cost reduction, durability, low iridium loading, proton exchange membrane water electrolysis

Received: June 6, 2025
Revised: September 30, 2025
Published online: November 26, 2025

[1] S. Chatterjee, X. Peng, S. Intikhab, G. Zeng, N. N. Kariuki, D. J. Myers, N. Danilovic, J. Snyder, *Adv. Energy Mater.* **2021**, *11*, 2101438.
[2] M. van der Spek, C. Banet, C. Bauer, P. Gabrielli, W. Goldthorpe, M. Mazzotti, S. T. Munkejord, N. A. Røkke, N. Shah, N. Sunny, D. Sutter, J. M. Trusler, M. Gazzani, *Energy Environ. Sci.* **2022**, *15*, 1034.
[3] IEA, *Integrating Solar and Wind Global Experience and Emerging Challenges*, IEA, Paris **2024**.
[4] M. Chatenet, B. G. Pollet, D. R. Dekel, F. Dionigi, J. Deseure, P. Millet, R. D. Braatz, M. Z. Bazant, M. Eikerling, I. Staffell, P. Balcombe, Y. Shao-Horn, H. Schäfer, *Chem. Soc. Rev.* **2022**, *51*, 4583.
[5] S. S. Kumar, H. Lim, *Sustain. Energy Fuels* **2023**, *7*, 3560.
[6] M. Clapp, C. M. Zalitis, M. Ryan, *Catal. Today* **2023**, *420*, 114140.
[7] K. Georgitzikis, U. Eynard, S. Bobba, F. Perpetuo Coelho, D. Ingoglia, E. Garbossa, *Platinum: Impact Assessment for Supply Security*, European Commission, Brussels **2023**.
[8] C. Minke, M. Suermann, B. Bensmann, R. Hanke-Rauschenbach, *Int. J. Hydrog. Energy* **2021**, *46*, 23581.
[9] International Energy Agency, *Sustainable and Responsible Critical Mineral Supply Chains Guidance for Policy Makers*, International Energy Agency, Paris **2023**.
[10] International Renewable Energy Agency, *Geopolitics of the Energy Transition: Critical Materials*, International Renewable Energy Agency, Abu Dhabi **2023**.
[11] M. Bernt, A. Siebel, H. A. Gasteiger, *J. Electrochem. Soc.* **2018**, *165*, F305.
[12] T. Smolinka, N. Wiebe, P. Sterchele, A. Palzer, F. Lehner, M. Jansen, S. Kiemel, R. Miehe, S. Wahren, F. Zimmermann, *Studie IndWEDe Industrialisierung der Wasser elektrolyse in Deutschland: Chancen und Herausforderungen für nachhaltigen Wasserstoff für Verkehr*, Strom und Wärme, Berlin **2018**.
[13] E. Price, *Johnson Matthey Technol. Rev.* **2017**, *61*, 47.
[14] N. Utsch, M. Shviro, W. Lehnert, *ECS Meet. Abstr.* **2021**, *MA2021-02*, 1053.
[15] D. Hoffmeister, S. Finger, R. Pokhrel, A. Körner, B. Fritsch, S. Thiele, A. Hutzler, C. van Pham, *Chem. Eng. J.* **2025**, *517*, 164281.
[16] B. E. Hayden, *Acc. Chem. Res.* **2013**, *46*, 1858.
[17] L. M. Roen, C. H. Paik, T. D. Jarvi, *Electrochem. Solid-State Lett.* **2004**, *7*, A19.
[18] R. E. Fuentes, J. Farell, J. W. Weidner, *Electrochem. Solid-State Lett.* **2011**, *14*, E5.
[19] L. Wang, P. Lettenmeier, U. Golla-Schindler, P. Gazdzicki, N. A. Cañas, T. Morawietz, R. Hiesgen, S. S. Hosseiny, A. S. Gago, K. A. Friedrich, *Phys. Chem. Chem. Phys.* **2016**, *18*, 4487.
[20] J. Xu, G. Liu, J. Li, X. Wang, *Electrochim. Acta* **2012**, *59*, 105.

[21] V. K. Puthiyapura, M. Mamlouk, S. Pasupathi, B. G. Pollet, K. Scott, *J. Power Sources* **2014**, *269*, 451.
[22] L. Ma, S. Sui, Y. Zhai, *J. Power Sources* **2008**, *177*, 470.
[23] B. Han, M. Risch, S. Belden, S. Lee, D. Bayer, E. Mutoro, Y. Shao-Horn, *J. Electrochem. Soc.* **2018**, *165*, F813.
[24] Y. Liu, T. G. Kelly, J. G. Chen, W. E. Mustain, *ACS Catal.* **2013**, *3*, 1184.
[25] F. Karimi, B. A. Peppley, *Electrochim. Acta* **2017**, *246*, 654.
[26] G. Koderman Podborsek, L. Suhadolnik, A. Loncar, M. Bele, A. Hrnjic, Z. Marinko, J. Kovac, A. Kokalj, L. Gasparic, A. K. Surca, A. R. Kamsek, G. Drazic, M. Gaberscek, N. Hodnik, P. Jovanovic, *ACS Catal.* **2022**, *12*, 15135.
[27] E. Antolini, E. R. Gonzalez, *Solid State Ionics* **2009**, *180*, 746.
[28] L. Moriau, M. Smiljanić, A. Lončar, N. Hodnik, *ChemCatChem* **2022**, *14*, e202200586.
[29] H. S. Oh, H. N. Nong, T. Reier, A. Bergmann, M. Gliech, J. Ferreira De Araújo, E. Willinger, R. Schlögl, D. Teschner, P. Strasser, *J. Am. Chem. Soc.* **2016**, *138*, 12552.
[30] A. Hartig-Weiss, M. Miller, H. Beyer, A. Schmitt, A. Siebel, A. T. S. Freiberg, H. A. Gasteiger, H. A. El-Sayed, *ACS Appl. Nano Mater.* **2020**, *3*, 2185.
[31] V. A. Saveleva, E. R. Savinova, *Curr. Opin. Electrochem.* **2019**, *17*, 79.
[32] I. A. Khan, P. Morgen, S. Gyergyek, R. Sharma, S. M. Andersen, *Mater. Chem. Phys.* **2023**, *308*, 128192.
[33] H. S. Oh, H. N. Nong, T. Reier, M. Gliech, P. Strasser, *Chem. Sci.* **2015**, *6*, 3321.
[34] Y. C. Chiang, Z. H. Pu, Z. Wang, *Nano* **2023**, *13*, 2264.
[35] N. Sergent, P. Gélin, L. Périer-Camby, H. Praliaud, G. Thomas, *Sens. Actuators B Chem.* **2002**, *84*, 176.
[36] Geiger, S., Kasian, O., Mingers, A. M., Mayrhofer, K. J. J., Cherevko, S., *Sci.Rep.* **2017**, *7*, 4595.
[37] G. Liu, J. Xu, Y. Wang, X. Wang, *J. Mater. Chem. A* **2015**, *3*, 20791.
[38] X. Geng, M. Vega-Paredes, Z. Wang, C. Ophus, P. Lu, Y. Ma, S. Zhang, C. Scheu, C. H. Liebscher, B. Gault, *Nat. Commun.* **2024**, *15*, 8534.
[39] K. Rubenis, S. Populoh, P. Thiel, S. Yoon, U. Müller, J. Locs, *J. Alloys Compd.* **2017**, *692*, 515.
[40] R. H. Schröder, N. Schmitz-Pranghe, R. Kohlhaas, *Int. J. Mater. Res.* **2021**, DOI: 10.1515/ijmr-1972-630103.
[41] A. Marshall, B. Børresen, G. Hagen, S. Sunde, M. Tsypkin, R. Tunold, *Russ. J. Electrochem.* **2006**, *42*, 1134.
[42] O. Vodeb, A. Lončar, M. Bele, A. Hrnjić, P. Jovanovič, M. Gaberščček, N. Hodnik, *Electrochim. Acta* **2023**, *464*, 142882.
[43] C. Rakousky, U. Reimer, K. Wippermann, M. Carmo, W. Lueke, D. Stolten, *J. Power Sources* **2016**, *326*, 120.
[44] S. Siracusano, S. Trocino, N. Briguglio, F. Pantò, A. S. Aricò, *J. Power Sources* **2020**, *468*, 228390.
[45] M. Möckl, M. F. Ernst, M. Kornherr, F. Allebrod, M. Bernt, J. Byrknes, C. Eickes, C. Gebauer, A. Moskovtseva, H. A. Gasteiger, *J. Electrochem. Soc.* **2022**, *169*, 064505.
[46] P. Lettenmeier, R. Wang, R. Abouatallah, S. Helmly, T. Morawietz, R. Hiesgen, S. Kolb, F. Burggraf, J. Kallo, A. S. Gago, K. A. Friedrich, *Electrochim. Acta* **2016**, *210*, 502.
[47] T. Schuler, R. De Bruycker, T. J. Schmidt, F. N. Büchi, *J. Electrochem. Soc.* **2019**, *166*, F270.
[48] T. C. Ma, A. Hutzler, R. Hanke-Rauschenbach, S. Thiele, *Electrochem. Commun.* **2025**, *178*, 107965.
[49] H. Yu, L. Bonville, J. Jankovic, R. Maric, *Appl. Catal. B* **2020**, *260*, 118194.
[50] J. Torrero, T. Morawietz, D. García Sanchez, D. Galyamin, M. Retuerto, V. Martin-Diaconescu, S. Rojas, J. A. Alonso, A. S. Gago, K. A. Friedrich, *Adv. Energy Mater.* **2023**, *13*, 2204169.
[51] C. Liu, M. Shviro, G. Bender, A. S. Gago, T. Morawietz, M. J. Dzara, I. Biswas, P. Gazdzicki, Z. Kang, S. F. Zaccarine, S. Pylypenko, K. A. Friedrich, M. Carmo, W. Lehnert, *J. Electrochem. Soc.* **2023**, *170*, 034508.
[52] S. Siracusano, V. Baglio, S. A. Grigoriev, L. Merlo, V. N. Fateev, A. S. Aricò, *J. Power Sources* **2017**, *366*, 105.
[53] D. Jalalpoor, D. Göhl, P. Paciok, M. Heggen, J. Knossalla, I. Radev, V. Peinecke, C. Weidenthaler, K. J. J. Mayrhofer, M. Ledendecker, F. Schüth, *J. Electrochem. Soc.* **2021**, *168*, 024502.
[54] S. J. Freakley, J. Ruiz-Esquius, D. J. Morgan, *Surf. Interface Anal.* **2017**, *49*, 794.
[55] V. Pfeifer, T. E. Jones, J. J. Velasco Vélez, C. Massué, R. Arrigo, D. Teschner, F. Girgsdies, M. Scherzer, M. T. Greiner, J. Allan, M. Hashagen, G. Weinberg, S. Piccinin, M. Hävecker, A. Knop-Gericke, R. Schlögl, *Surf. Interface Anal.* **2016**, *48*, 261.
[56] N. Danilovic, R. Subbaraman, K. C. Chang, S. H. Chang, Y. J. Kang, J. Snyder, A. P. Paulikas, D. Strmcnik, Y. T. Kim, D. Myers, V. R. Stamenkovic, N. M. Markovic, *J. Phys. Chem. Lett.* **2014**, *5*, 2474.
[57] S. Geiger, O. Kasian, B. R. Shrestha, A. M. Mingers, K. J. J. Mayrhofer, S. Cherevko, *J. Electrochem. Soc.* **2016**, *163*, F3132.
[58] M. Milosevic, T. Böhm, A. Körner, M. Bierling, L. Winkelmann, K. Ehelebe, A. Hutzler, M. Suermann, S. Thiele, S. Cherevko, *ACS Energy Lett.* **2023**, *8*, 2682.
[59] P. Lettenmeier, J. Majchel, L. Wang, V. A. Saveleva, S. Zafeiratos, E. R. Savinova, J. J. Gallet, F. Bournel, A. S. Gago, K. A. Friedrich, *Chem. Sci.* **2018**, *9*, 3570.
[60] J. Rodriguez-Carvajal, *Phys. B Condens. Matter* **1993**, *192*, 55.
[61] L. Simonelli, C. Marini, W. Olszewski, M. Ávila Pérez, N. Ramanan, G. Guilera, V. Cuartero, K. Klementiev, *Cogent Physics* **2016**, *3*, 1231987.
[62] B. Ravel, M. Newville, *J. Synchrotron Radiat.* **2005**, *12*, 537.
[63] G. Bender, M. Carmo, T. Smolinka, A. Gago, N. Danilovic, M. Mueller, F. Ganci, A. Fallisch, P. Lettenmeier, K. A. Friedrich, K. Ayers, B. Pivovar, J. Mergel, D. Stolten, *Int. J. Hydrog. Energy* **2019**, *44*, 9174.
[64] C. Liu, M. Shviro, A. S. Gago, S. F. Zaccarine, G. Bender, P. Gazdzicki, T. Morawietz, I. Biswas, M. Rasinski, A. Everwand, R. Schierholz, J. Pfeilsticker, M. Müller, P. P. Lopes, R. A. Eichel, B. Pivovar, S. Pylypenko, K. A. Friedrich, W. Lehnert, M. Carmo, *Adv. Energy Mater.* **2021**, *11*, 2002926.